RSC Advances

ROYAL SOCIETY OF CHEMISTRY

www.rsc.org/advances

Fe-Doped Anatase TiO_2/Carbon Composite as Anode with Superior Reversible Capacity for Lithium Storage

Yanqing Lai, Wenwen Liu, Jing Fang, Furong Qin, Mengran Wang, Fan Yu, Kai Zhang*

School of Metallurgy and Environment, Central South University, 932 Lushan South Road, Changsha 410083, PR China

* Corresponding author: chinamcsu@163.com (Kai Zhang)

Abstract: This paper reports an economic and effective wet chemistry process to prepare Fe-doped anatase TiO_2/carbon composite with excellent performance in lithium-ion batteries. The as-prepared materials possess large BET specific area and high conductivity, owing to the existence of iron and carbon, which is conducive to electrolyte permeation and in favor of accelerating the electrochemical kinetics. When used as anode materials for advanced lithium storage, it leads to much better electrochemical performance than the pure TiO_2, delivering an initial discharge capacity of 381.7 mA h g^{-1} with a drop of less than 1% from the 2^{nd} cycle to the 300^{th} cycle at a high current density of 10 C (1 C = 170 mA g^{-1}).

Keywords: Fe doped; Anatase TiO_2; Carbon composite; Lithium storage

Introduction

In order to meet the demands of various types of future portable electronic devices, essential efforts have been made to develop advanced lithium ion batteries (LIBs) in the past few years [1, 2]. Graphite as the most common anode materials have been widely applied in commercial LIBs. However, it is easy to form lithium dendrite and thermally instable of solid-electrolyte interphase (SEI) film because of its low operating voltage (below 0.2 V vs Li/Li^+), thus causing safety hazards and capacity fading [3, 4]. In this regard, TiO_2 has received considerable attention as a replaceable anode material for graphite, due to its unique features, including low cost, environmental benignity, small volume change (< 4%), good cycling stability and high discharge voltage plateau (above 0.8 V vs Li/Li^+) [5-7]. Different kinds of polymorphs of titania such as anatase, rutile and TiO_2 (B) have recently been investigated as anode materials for LIBs [8]. Among the three common crystal forms of TiO_2, anatase is the most extensively studied, because of its stable crystal phase of nanometer dimensions [9]. Nevertheless, it presents poor ionic and electrical conductivity, which will limit its real performance in LIBs. More seriously, anatase TiO_2 offers a low theoretical capacity of 170 mA h g^{-1}, which directly affects its commercial application [10].

So as to address the above issues, researchers have taken a myriad of effective strategies. The most popular way is to tune the shape at the nanoscale [11, 12] (hollow sphere [13], nanotube [14], nanosheet [10, 15], etc), because these morphologies with higher specific surface areas can support more active surface sites compared with solid counterparts. Another widely-used measure is to incorporate with secondary phase, such as graphene [16, 17], Ag [18], iron oxide [19] and NiO [20, 21], owing to their superior electronic conductivity or higher theoretical capacity. However, it is typically difficult to provide a durable and homogeneous electron transport path that blankets the entire surface of the particles [22]. Moreover, these methods always require too many sophisticated processes to ensure materials uniformity and integrity. Recently, heterogeneous element doping (B [23], C [24], Fe [25], F^- [26] etc) has also aroused increasing interests in the field of LIBs, and it has been confirmed to exhibit improved capacity and rate capability. Substitutional doping of TiO_2 presents a quite challenging obstacle in thermodynamic solubility on account of low solubility for most dopants. Only when most of them are located in desirable position, may it be helpful for providing mobile charge carriers [27]. Taking these reasons into consideration, combining the merits of carbon and doping, such as fluorine-doped carbon coated mesoporous TiO_2 [28] and N-doped TiO_2 nanorods decorated with carbon dots [29], has been reported. The researches also show that, to a great degree, it is indeed possible to

improve the electrochemical properties of lithium-ion batteries. Specifically, Ji et.al. [29] have demonstrated that carbon dots supported upon N-doped TiO_2 nanorods can sustain a capacity of 185 mA h g^{-1} with 91.6% retention even at a high rate of 3350 mA g^{-1} over 1000 cycles. To the best of our knowledge, so far, Fe-doped anatase TiO_2/carbon composites have not been used as anode materials in LIBs.

Herein, we report a wet chemistry process to obtain Fe-doped anatase TiO_2/carbon composite (FC-TiO_2) with high rate capability for the high power application of LIBs, where substitutional Fe atoms for lattice Ti, locate in the bulk and the surface layer of the crystals. Meanwhile, the remaining of carbon decorates on the composites. The doping of iron could not only restrain the growth of TiO_2 crystallite so that form tiny particles, but also largely narrow the band gap, thus enhancing the conductivity of TiO_2. Additionally, the carbon in the FC-TiO_2 can support a conductive secondary phase. Based on these improvements, the FC-TiO_2 micro-materials display excellent electrochemical performances, such as a high capacity around 222.4 mA h g^{-1} at the current rate of 3 C and a reversible capacity over 158 mA h g^{-1} after 300 cycles at the heavy current rate of 10 C.

Experimental section

Materials and synthesis

The synthesis of Fe-doped anatase TiO_2/carbon composite was accomplished via a wet chemistry process, which involves hydrolysis of tetrabutyl titanate (TBT) in a mixture of ethylene glycol and $FeCl_3$ $6H_2O$, followed by heating at 500 ℃ (**Fig 1**). Typically, 50 mL of ethylene glycol and 0.48 g of $FeCl_3$•$6H_2O$ were well blended in a beaker, and then 5 mL of TBT was added to the well-distributed yellow solution with vigorous mechanical stirring. Afterward, it was transferred into an electric oven and heated at 180 ℃ for 5 h. When it cooled to room temperature, the yellow precipitate was collected and rinsed with anhydrous alcohol several times until the filtrate turned colorless and clear. After being dried at 70 ℃ in a conventional oven for 12 h, one portion of the as-prepared sample was calcined in a tube furnace at 500 ℃ for 2 h under an air atmosphere, which was aimed to remove carbon element. The sample was signed as F-TiO_2. Meanwhile, the residual was heated under an argon atmosphere, while the temperature and time kept the same, labeled as FC-TiO_2. As comparison, the TiO_2/carbon composite (C-TiO_2) and pure TiO_2 were also been prepared under otherwise identical conditions, just without $FeCl_3$•$6H_2O$ as addictive.

Sample characterization

The morphological analyses were characterized by a scanning electron microscope (SEM, JEOL, JSM-5612LV) and STEM (Tecnai G2 F20). The as-prepared specimens were characterized by X-ray diffraction (XRD, Rigaku3014) which were made with Cu Kα radiation. X-ray photoelectron spectroscopy (XPS, ESCA LAB 250Xi) was utilized to analyze the chemical state in the FC-TiO_2 material. N_2 adsorption–desorption (Micrometrics ASAP 2020) measurements were employed to investigate the textural properties. The surface area and the pore size distribution was analyzed by the Brunauer–Emmett–Teller (BET) and the Barrett–Joyner–Halenda (BJH) method, respectively. The carbon content in the FC-TiO_2 composite was measured by high frequency infrared ray carbon sulphur analyser (CS-600, US) and thermo-gravimetric analysis (TGA, SDT Q600). Inductively coupled plasma-atomic emission spectrometer (ICP-AES, Thermo Electron corporation, US) was conducted in determining the concentration of iron.

Electrochemical Measurements

The electrochemical performances were carried out in CR2025 coin-type cells with a lithium plate serving as the counter and reference electrode. The

working electrodes were prepared by casting the homogeneous slurry in which the obtained samples were mixed with super-P and polyvinylidene fluoride (PVDF) at a weight ratio of 70:20:10 in N-methyl pyrrolidinone (NMP) on the copper foil current collector. The electrodes were dried under vacuum at 60 ℃ overnight and then pressed into disks (10 mm, diameter). The cells were assembled in a dry and high-purity argon-filled glove box, employing 1 M $LiPF_6$ in ethylene carbonate (EC), dimethyl carbonate (DMC), diethyl carbonate (DEC) with a volume ratio of 1:1:1 as electrolyte and celgard-2400 as separator. Galvanostatic testing was carried out with LAND battery circler over the voltage range of 3.0 to 0.01 V (vs. Li^+/Li). Cyclic voltammetry (CV) tests were recorded at a scan rate of 0.02 mV S^{-1} in the voltage range from 0.01 to 3.0 V. The electrochemical impedance spectroscopy (EIS) measurements were conducted using PARSTAT 2273 electrochemical measurement system, and they were carried out at opencircuit potential by applying an AC voltage of 5 mV amplitude in the 0.01 Hz–100 kHz frequency range. All these tests were operated in the room temperature (25℃).

Results and discussion

The morphologies of pure TiO_2 and modified TiO_2 powders are shown in **Fig 2. Fig 2a-2d** display the SEM images of the whole as-prepared

samples. It is obvious that all of them possess similar micro-structures that looks like irregular prism structure. After being modified by carbon and iron, the length and width of the prism slightly decreased. From the TEM images of FC-TiO_2 (**Fig 2e**), many pores can be found.

In order to ulteriorly confirm the specific surface area of all the materials and the diameter of these pores, the N_2 adsorption–desorption isotherm curves (**Fig 3**) of all the specimen have been investigated. It can be clearly showed from the images that they show a well-defined adsorption step and exhibit a typical type-IV isotherm, which is aimed at determining the BET surface area (**Fig 3a**) and BJH pore size distribution (**Fig 3b**). Apparently, all of them represent the mesoporous characteristics. The F-TiO_2 has the highest BET specific surface area of 66.07 m^2 g^{-1}, which is almost 1.8 times higher than that of pure TiO_2 samples of 38.02 m^2 g^{-1}. After the F-TiO_2 and the pure TiO_2 samples being modified by carbon, their BET specific surface area has a little decline, about 52.27 m^2 g^{-1} for FC-TiO_2 and 27.66 m^2 g^{-1} for C-TiO_2. As it can be seen from the BJH pore size distribution (**Fig 3b**), all of them display an unimodal peak. With the exception of the C-TiO_2, the majority of pores of other three samples is around 5-15 nm. This may be ascribed that when the pure TiO_2 is modified by carbon, a part of carbon will cover the inside of the mesoporous, thus decreasing the pore size and the specific surface area.

As shown in **Fig 2f**, thermo gravimetric analysis (TGA) was performed to investigate the accurate carbon content in the FC-TiO_2 composite. The TGA curve depicts the rate of weight of the FC-TiO_2 composite under air atmosphere. On the basis of TGA curve, three thermal events can be observed. The first 8.58% mass loss below 300 ℃ is contributed to the evaporation of residual ethanol and moisture. With the temperature further increasing, the second 14.56% mass loss in the range from 300 to 450 ℃ is assigned to the oxidation of carbon which is coated on the surface of the FC-TiO_2 composite [30]. The last 1.8% mass loss between 600 and 800 ℃ could correspond to the oxidation of residual carbon forming a Ti-O-C structure, which agrees with the XPS spectrogram (**Fig 4c**). However, iron and titanium will be oxidized in the air, thus making the weight of the material increase, which means the carbon content measured by TGA is a little higher than the actual weight. Therefore, high frequency infrared ray carbon sulphur analyser (CS600) is used to investigate the accurate carbon content. According to the result, 13.34 wt% carbon is found in the composite. Moreover, according to the ICP result, it reveals that there is only 0.18 wt% iron in the composite. Therefore, more than 85 wt% is titanium and oxygen.

Fig 4a shows the XRD patterns of the whole samples, revealing that the TiO_2 crystals are indexed to an anatase phase (JCPDS no. 21-1272),

except for C-TiO_2. It is obvious that the peak of C-TiO_2 is too broad to identify the phases correctly, but they are strikingly similar to the poor crystalline carbon [30]. Moreover, there is no reflection corresponding to titanium oxide seeing in the XRD pattern because of the loss of crystallinity or formation of amorphous structures during pyrolysis. Additionally, for pure TiO_2 samples, there is a small peak at 27.4 °which is from rutile phase. But for other modified samples, the peak disappears. These evidences imply that the crystalline phase slightly changes during the recombination process. Further observation shows that, in contrast to pure TiO_2, the XRD peak intensities of the FC-TiO_2 anatase steadily become weaker and the width of the XRD diffraction peaks of the FC-TiO_2 anatase becomes slightly wider, indicating that the smaller TiO_2 crystallites has formed and the degree of crystallinity has decreased [31]. This is ascribed to the facts that Fe substitution not only lowers the crystallization of TiO_2 but also slightly restrains the growth of TiO_2 crystallite [32].

In order to determine the composition and identify the chemical states of FC-TiO_2, X-ray photoelectron spectroscopy (XPS) analysis was also carried out. The high resolution XPS results are shown in **Fig 4b-f**. From the XPS survey spectra of FC-TiO_2 (**Fig 4b)**, Ti, O, Fe, and C are easily found on the surface of the composite, which together with XRD (**Fig 4a**) and the

corresponding energy-dispersive X-ray spectroscopy (EDS) mapping (**Fig 5**) confirmed that the Fe, C atoms are uniformly dispersed inside the TiO_2 micro particles. The carbon state in FC-TiO_2 was assessed by C 1s core levels, in which the C 1s peaks can be fitted as three peaks at binding energies of 284.6, 285.1 and 289 eV, as shown in **Fig 5C**. The first two value are assigned to adventitious carbon contamination, which cannot be eliminated [33]. While the last one implies the presence of C–O bonds [34], and the data reveals that the carbon may be incorporated into the interstitial positions of the TiO_2 lattice [33] or substitute for some of the lattice atoms [35, 36] and form a Ti-O-C structure, which is well consistent with the TGA curve. **Fig 4d** presents the O 1s XPS spectra of FC-TiO_2. One accurate peak of O 1s is located at about 530.4 eV, whose energy is equal to the O 1s electron binding energy for TiO_2, corresponding to lattice oxygen of TiO_2 [37]. Two peaks of Ti 2p3/2 and Ti 2p1/2 at 459.3 eV and 464.9 eV with better symmetry are shown in the high-resolution XPS spectrum (**Fig 4e**), which are assigned to the lattice titanium in TiO_2 [38]. Between these two peaks, there is a separation distance about 5.6 eV, which agrees well with the energy reported for TiO_2 [39]. On account of the low doping level, the Fe signals are quite weak. These results can be easily found in the higher solution XPS spectra of the Fe 2p3/2 region (**Fig 4f**). However, there is still a obvious peak located at 714.4 eV. It can be ascribed to Fe^{3+} ion [40]. It is

clear that this is not because of Fe^{3+} in Fe_2O_3 (at 715.7 eV) [41], but because of the $FeCl_3$•$6H_2O$ dopant. Since the radius of Fe^{3+} is similar with Ti^{4+}, the Fe^{3+} could be incorporated into the lattice of TiO_2, forming Ti–O–Fe bonds in the FC-TiO_2 micro-particles after calcination [31].

Various preliminary electrochemical characterizations of the as-synthesized FC-TiO_2 particles with respect to Li insertion/extraction were carried out to evaluate potential applicability in the lithium storage. The insertion and extraction of lithium to and from the anatase lattice proceeds according to the equation:

$$TiO_2 + nLi^+ + ne^- \leftrightarrow Li_nTiO_2$$

When n equals 1, the theoretical capacity of TiO_2 will obtain 336 mA h g^{-1}. In general, the insertion coefficient n is close to 0.5 in anatase at a slower charge/discharge process [42]. It is described by the space group $I4_1/amd$ that the anatase phase has a tetragonal structure [43]. A Ti ion is surrounded by a distorted oxygen octahedron. Between these octahedrons, there are plenty of vacant octahedral and tetrahedral sites in which Li^+ ions are accommodated. Moreover, it is worth noting that it will result in a phase transition from a Li-poor (tetragonal) phase to a Li-rich (orthorhombic, cubic spinel, cubic rocksalt, etc.) phase with Li-ion insertion [44].

Fig 6a highlights the typical charge/discharge voltage profiles of the FC-TiO_2 electrode for the 1st, 2nd, 3rd and 50th cycles at a current rate of 3 C between 0.01 and 3.0 V. As a result, although a high capacity of 486.4 mA h g^{-1} (corresponding to an n-value of 1.45) can be delivered in the initial discharge, the corresponding charge capacity is only 199.3 mA h g^{-1}. In the comparative experiment, the pure TiO_2 has a lower capacity of 364 mA h g^{-1} in the first discharge with the corresponding charge capacity of 122.8 mA h g^{-1} (**Fig 6b**). The large capacity loss in the initial cycle may mainly result from the interfacial reaction between TiO_2 and the electrolyte, which is common to most lithium intercalation hosts [45]. Moreover, the irreversible capacity decay may reflect the poor intrinsic conductivity of TiO_2. Upon lithium extraction, the surface region of TiO_2 will become highly insulating [45]. Noting that the initial coulombic efficiency of FC-TiO_2 (40.97%) is higher than that of pure TiO_2 (33.74%), the fact could attribute to the carbon decorated on the surface of TiO_2. On one hand, it can reduce the conduct areas between TiO_2 and electrolyte to decrease the irreversible side effects [46]. On the other hand, it can improve the conductivity of TiO_2, thus increasing the extent of the reverse reaction in the initial charge process [47]. Fortunately, from the second cycle, the charge/discharge curves are almost identical, suggesting that the electrochemical process is stable during the lithium-insertion/extraction reactions**. Fig 6c** and **6d** show the cyclic

voltammograms (CV) of FC-TiO_2 and TiO_2 electrodes measured at a scanning rate of 0.02 mV s^{-1} for the first two scans. Obviously, in each scan there is one apparent single pair of sharp cathodic/anodic peaks for Li-ion intercalation/deintercalation processes on the CV plots of both the two samples [48]. They are located at ~1.6 and ~2.1 V for pure TiO_2, ~1.7 and ~1.95 V for FC-TiO_2, respectively. It is clear that the separation between reduction and oxidation peaks (ΔV) of FC-TiO_2 markedly decreases in contrast to that of the pure TiO_2, which means the existence of iron and carbon can reduce the polarization of the anode/electrolyte interface in Li-ion batteries and leads to a better charge/discharge reversibility of TiO_2 [43]. On the other hand, it also exhibits a small irreversible capacity and relatively little difference between the first and the second scans, implying that this electrode possesses excellent cycling stability and reversibility.

The electrochemical properties of modified and pure TiO_2 were investigated in lithium half-cells. As shown in **Fig 7,** all the modified samples shows higher performance than that of pure TiO_2, with the FC-TiO_2 specimen possessing the highest specific capacity and the best cycling performance. Clearly, **Fig 7a** exhibits the cycling performance of all the obtained samples at a constant current density of 3 C. After 50 cycles, a preponderant cyclic retention of FC-TiO_2 with perfect reversible capacity of

222.8 mA h g^{-1} is significantly higher than that of C-TiO_2 and F-TiO_2 (135.4 and 124.6 mA h g^{-1}, respectively), even twice larger than that of TiO_2 (103.4 mA h g^{-1}). More importantly, its coulombic efficiency approaches almost 100% after first several cycles. This outcome shows that when TiO_2 is only modified by carbon or doped with iron followed by using as anode for LIBs, the electrochemical performance of them has a little improved. In addition, comparing with the pure TiO_2 sample, the FC-TiO_2 sample demonstrates more outstanding capacity retention of 158.6 mA h g^{-1} at a heavy current rate of 10 C after a long-term cycling performance of 300 cycles, with an irreversible capacity loss of less than 1% after the second cycle (**Fig 8a**), which is at a relatively high level by comparing with those of the reported anode materials. The details are described in the **Table 1**.The results can be attribute to relatively high surface area, which is conducive to electrolyte permeation and in favor with accelerating the electrochemical kinetics. Furthermore, the FC-TiO_2 also exhibits excellent rate capability at charge/discharge current rates ranging from 1 to 20 C, as shown in **Fig 7b**. High capacities of 306.1, 234.2, 208.1, 165.1, 124.6 and 95.5 mA h g^{-1} can be delivered at current rates of 1, 2, 3, 5, 10 and 20 C, respectively, which is the highest among all the samples. More importantly, a stable high discharge capacity of 208.6 mA h g^{-1} can be attained when the current density is switched back to 3 C. These results explicitly testify the excellent lithium

storage performances of FC-TiO_2 in terms of long cycle life and a good rate capability for the fast charging/discharging process. In brief, comparing with pure TiO_2, more outstanding electrochemical performance of the as-prepared FC-TiO_2 as anode materials for LIBs can be ascribed to several perspectives. First, the smaller impedance can be favor with accelerating the electrochemical kinetics. Second, the higher BET specific surface provides enough surface sites and electrolyte/electrode interface, which ensures a better penetration of electrolyte so that it is helpful to lower current densities at the electrode/electrolyte interface. Additionally, the more porous structure can shorten the transmission distance of Li^+, thus speeding up the rate of lithium insertion and extraction. All these features can explain why FC-TiO_2 provides improved electrochemical process and offers high specific capacity especially at high current rates.

To further verify the improved electrochemical performance of FC-TiO_2 micro particles, electrochemical impedance spectroscopy (EIS) was carried out for the FC-TiO_2 and pure TiO_2 cathodes before cycling with frequency from 0.01 Hz to 100 kHz, and both of the ac impedance spectrums are illustrated in **Fig 8b**. As it can be seen, the Nyquist plots of both electrodes are characteristic of a semicircle at high frequency, corresponding to the absence of a SEI layer on the electrode surface, as well as an inclined

line in the low frequency region, reflecting the solid-state diffusion of Li-ions within the electrode [24]. Apparently, the charge-transfer resistance of FC-TiO_2 electrode is lower than that of pure TiO_2 electrode, it can be ascribed to the existence of iron [25] and carbon [49] in the TiO_2 micro-particles.

Conclusions

In summary, Fe-doped anatase TiO_2/carbon composite with superior reversible capacity has been successfully synthetized by a facile and economic wet chemistry process. Compared with pure TiO_2, the as-prepared FC-TiO_2 not only provides with a large BET specific surface area and a high pore volume, but also it possesses improved conductivity. As an anode material for advanced lithium storage, it exhibits high capacity and good capacity retention. This great improvement is attributed to the optimization of the material design in the composition, which can advance the commercial use of TiO_2 anode materials.

Acknowledgments

The research leading to these results has received funding from the China Postdoctoral Science Foundation funded project (2015M570685) and National Natural Science Foundation of China (Grant no. 51404304), Natural Science Foundation of Hunan Province (14JJ2001). The authors also

thank the Fundamental Research Funds for the Central Universities of Central South University (2015zzts186) and other supports from the Engineering Research Centre of Advanced Battery Materials, the Ministry of Education, China.

References

1. R. Marom, S. F. Amalraj, N. Leifer, D. Jacob and D. Aurbach, J. Mater. Chem, 2011, 21, 9938.
2. P. G. Bruce, B. Scrosati and J. M. Tarascon, Angew. Chem. Int. Ed. Engl., 2008, 47, 2930.
3. K. S. Novoselov, A. K. Geim, S. V. Morozov, D. Jiang, Y. Zhang, S. V. Dubonos, I. V. Grigorieva and A. A. Firsov, Science, 2004, 306, 666.
4. Y. Zhang, F. Du, X. Yan, Y. Jin, K. Zhu, X. Wang, H. Li, G. Chen, C. Wang and Y. Wei, ACS. Appl. Mater. Interfaces., 2014, 6, 4458.
5. J. S. Chen, L. A. Archer and X. Wen Lou, J. Mater. Chem., 2011, 21, 9912.
6. X. Chen and S. S. Mao, Chem. Rev., 2007, 2891.
7. D. Deng, M. G. Kim, J. Y. Lee and J. Cho, Energy. Environ. Sci., 2009, 2, 818.

8. D. Dambournet, I. Belharouak and K. Amine, Chem. Mater., 2010, 22, 1173.
9. C. L. Olson, J. Nelson and M. S. Islam, J. Phys. Chem. B., 2006, 110, 9995.
10. H. Hu, L. Yu, X. Gao, Z. Lin and X. W. Lou, Energy. Environ. Sci., 2015, 8, 1480.
11. X. Yang, Y. Yang, H. Hou, Y. Zhang, L. Fang, J. Chen and X. Ji, J. Phys. Chem. C., 2015, 119, 3923.
12. Y. G. Guo, Y. S. Hu, W. Sigle and J. Maier, Adv. mater., 2007, 19, 2087.
13. G. Zhang, H. B. Wu, T. Song, U. Paik and X. W. Lou, Angew. Chem. Int. Ed. Engl., 2014, 53, 12590.
14. H. Xiong, M. D. Slater, M. Balasubramanian, C. S. Johnson and T. Rajh, J. Phys. Chem. Lett., 2011, 2, 2560.
15. S. Liu, H. Jia, L. Han, J. Wang, P. Gao, D. Xu, J. Yang and S. Che, Adv. mater., 2012, 24, 3201.
16. W. Li, F. Wang, Y. Liu, J. Wang, J. Yang, L. Zhang, A. A. Elzatahry, D. Al-Dahyan, Y. Xia and D. Zhao, Nano. Lett., 2015, 15, 2186.
17. Z. Zhang, L. Zhang, W. Li, A. Yu and P. Wu, ACS. Appl. Mater. Interfaces., 2015, 7, 10395.

18. D. Fang, K. Huang, S. Liu and Z. Li, J. Alloys. Compd., 2008, 464, L5.
19. J. Lim, J. H. Um, J. Ahn, S. H. Yu, Y. E. Sung and J. K. Lee, Chem. Eur. J., 2015, 21, 7954.
20. L. P. An, X. P. Gao, G. R. Li, T. Y. Yan, H. Y. Zhu and P. W. Shen, Electrochim. Acta., 2008, 53, 4573.
21. S. H. Choi, J. H. Lee and Y. C. Kang, Nanoscale, 2013, 5, 12645.
22. Z. Bi, M. P. Paranthaman, B. Guo, R. R. Unocic, H. M. Meyer Iii, C. A. Bridges, X.-G. Sun and S. Dai, J. Mater. Chem. A, 2014, 2, 1818.
23. J.-H. Jeong, D.-w. Jung, E. W. Shin and E.-S. Oh, J. Alloys. Compd., 2014, 604, 226.
24. J. Xu, Y. Wang, Z. Li and W. F. Zhang, J. Power. Sources., 2008, 175, 903.
25. C. Andriamiadamanana, C. Laberty-Robert, M. T. Sougrati, S. Casale, C. Davoisne, S. Patra and F. Sauvage, Inorg. Chem., 2014, 53, 10129.
26. H.-G. Jung, C. S. Yoon, J. Prakash and Y.-K. Sun, J. Phys. Chem. C., 2009, 113, 21258.
27. S. B. Zhang, J. Phys. Condens. Matter., 2002, 14, R881.
28. H. Geng, H. Ming, D. Ge , J. Zheng and H. Gu, Electrochim. Acta. 2015, 157,1.

29. Y. Yang, X. Ji, M. Jing, H. Hou, Y. Zhu, L. Fang, X. Yang, Q. Chen and C. E. Banks, J. Mater. Chem. A., 2015, 3, 5648.

30. M.-H. Ryu, K.-N. Jung, K.-H. Shin, K.-S. Han and S. Yoon, J. Phys. Chem. C., 2013, 117, 8092.

31. J. Yu, Q. Xiang and M. Zhou, Appl. Catal. B., 2009, 90, 595.

32. L. Deng, S. Wang, D. Liu, B. Zhu, W. Huang, S. Wu and S. Zhang, Catal. Letters., 2009, 129, 513.

33. H. Li, D. Wang, H. Fan, P. Wang, T. Jiang and T. Xie, J. Colloid. Interface. Sci., 2011, 354, 175.

34. J. Droulas, T. M. Duc and Y. Jugnet, Le vide, les. couches. minces., 1991, 88, 39.

35. K. Palanivelu, J.-S. Im and Y.-S. Lee, Carbon. Lett., 2007, 8, 214.

36. X. Lin, F. Rong, X. Ji and D. Fu, Microporous. Mesoporous. Mater., 2011, 142, 276.

37. B. Dzhurinskii, D. Gati, N. Sergushin, V. Nefedov and Y. V. Salyn, Russ. J. Inorg. Chem., 1975, 20, 2307.

38. Y. Wang, T. Chen and Q. Mu, J. Mater. Chem., 2011, 21, 6006.

39. D. Briggs and M. P. Seah, D. Briggs, & M. P. Seah,(Editors), John Wiley & Sons, Chichester 1983, xiv+ 533, 1983.

40. V. Di Castro and S. Ciampi, Surf. sci., 1995, 331, 294.

41. R. Tandon, R. Payling, B. Chenhall, P. Crisp, J. Ellis and R. Baker, Appl. Surf. Sci., 1985, 20, 527.

42. X. D. Sun, C. L. Ma, Y. D. Wang and H. D. Li, Nanotechnology, 2004, 15, 1535.

43. D. Guan and Y. Wang, Ionics., 2012, 19, 879.

44. M. Vijayakumar, S. Kerisit, C. Wang, Z. Nie, K.M. Rosso, Z. Yang, G. Graff, J. Liu, J. Hu, J. Phys. Chem. C., 2009, 113, 14567.

45. S. Liu, Z. Wang, C. Yu, H. B. Wu, G. Wang, Q. Dong, J. Qiu, A. Eychmuller and X. W. David Lou, Adv. Mater., 2013, 25, 3462.

46. W. M. Zhang，X. L. Wu, J. S. Hu, Y. G. Guo, and L. J. Wan, Adv. Funct. Mater., 2008, 18, 3941.

47. Y. N. NuLi, Y. Q. Chu, and Q. Z. Qin, J. Electrochem. Soc.，2004, 15, A1077.

48. H. Ren, R. Yu, J. Wang, Q. Jin, M. Yang, D. Mao, D. Kisailus, H. Zhao and D. Wang, Nano. Lett.,2014, 14, 6679.

49. D. Gu, W. Li, F. Wang, H. Bongard, B. Spliethoff, W. Schmidt, C. Weidenthaler, Y. Xia, D. Zhao and F. Schuth, Angew. Chem. Int. Ed. Engl., 2015, 54, 7060.

50. M. Fehse, S. Cavaliere, P. E. Lippens, I. Savych, A. Iadecola, L. Monconduit, D. J. Jones, J. Rozière, F. Fischer, C. Tessier and L. Stievano, J. Phys. Chem. C., 2013, 117, 13827.

51. Y. Wang, M.Xu, Z. Peng and G. Zheng, J. Mater. Chem. A., 2013, 1, 13222.

52. M. Lübke, I. Johnson, N. M. Makwana, D. Brett, P. Shearing, Z. Liu, J. Darr, J. Power. Sources., 2015, 294, 94.

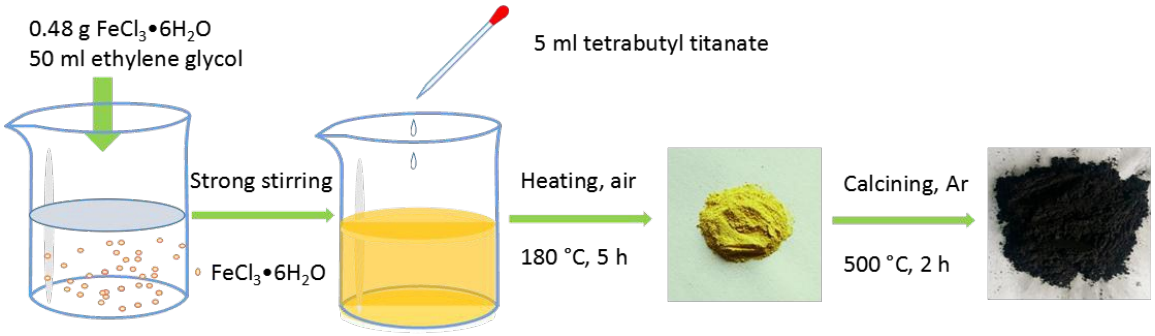

Fig 1. Illustration of the synthesis processes for FC-TiO_2.

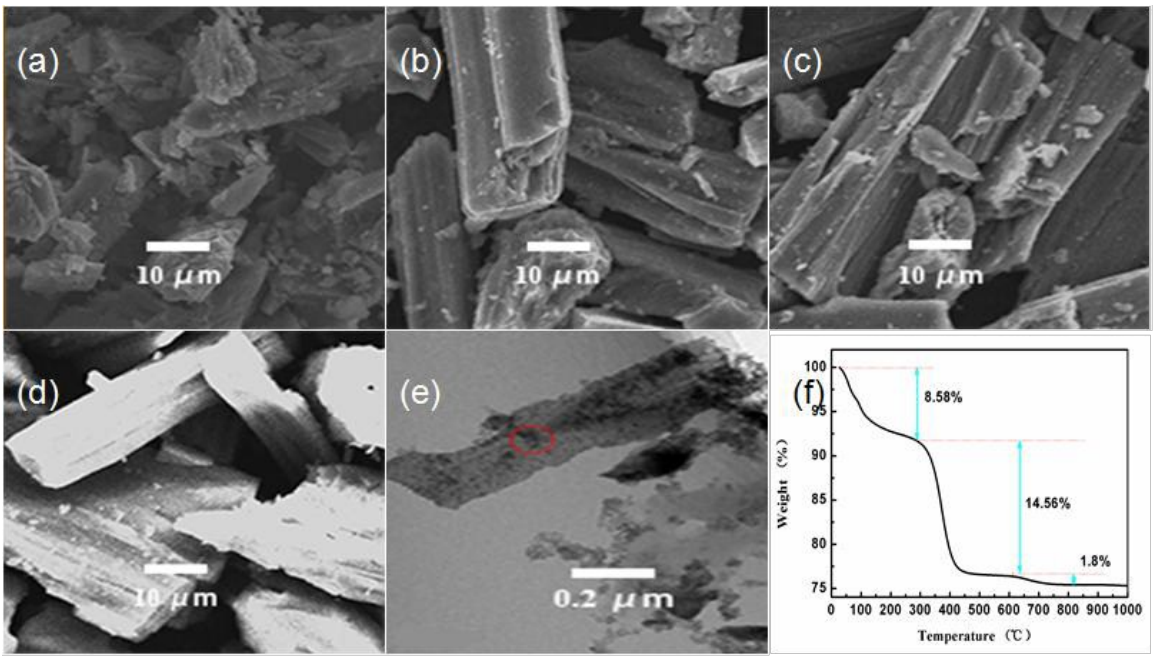

Fig 2. SEM images of **(a)** FC-TiO_2, **(b)** C-TiO_2, **(c)** F-TiO_2, **(d)** TiO_2 and **(e)** TEM image of FC-TiO_2; **(f)** TGA curve recorded for the FC-TiO_2 composite under air flow.

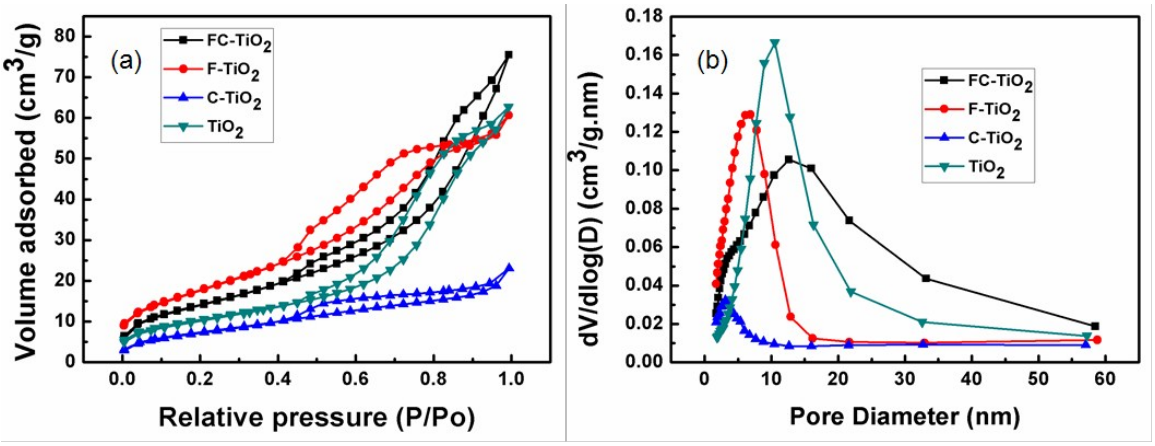

Fig 3. (a) Nitrogen adsorption and desorption isotherm and **(b)** pore size distribution of the whole pure and modified TiO_2.

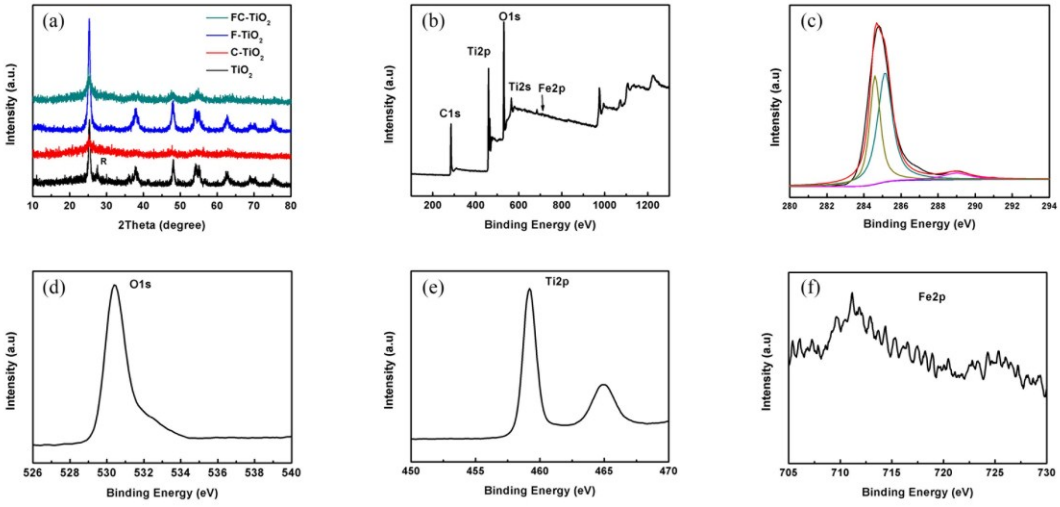

Fig 4. (a) Room temperature powder X-ray diffraction patterns of pure and modified TiO_2 micro-spheres. R: rutile. X-ray photoelectron spectroscopy (XPS) spectra of FC-TiO_2: **(b)** survey; **(c)** C 1s peaks; **(d)** O 1s peaks; **(e)** Ti 2p peaks and **(f)** Fe 2p peaks.

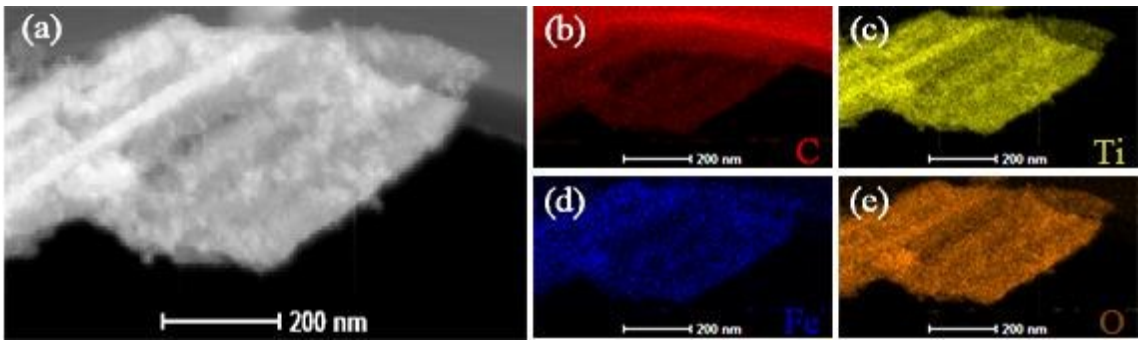

Fig 5. (a) ADF-STEM image of the FC-TiO_2 and the corresponding elemental mapping for **(b)** carbon, **(c)** titanium, **(d)** iron and **(e)** oxygen.

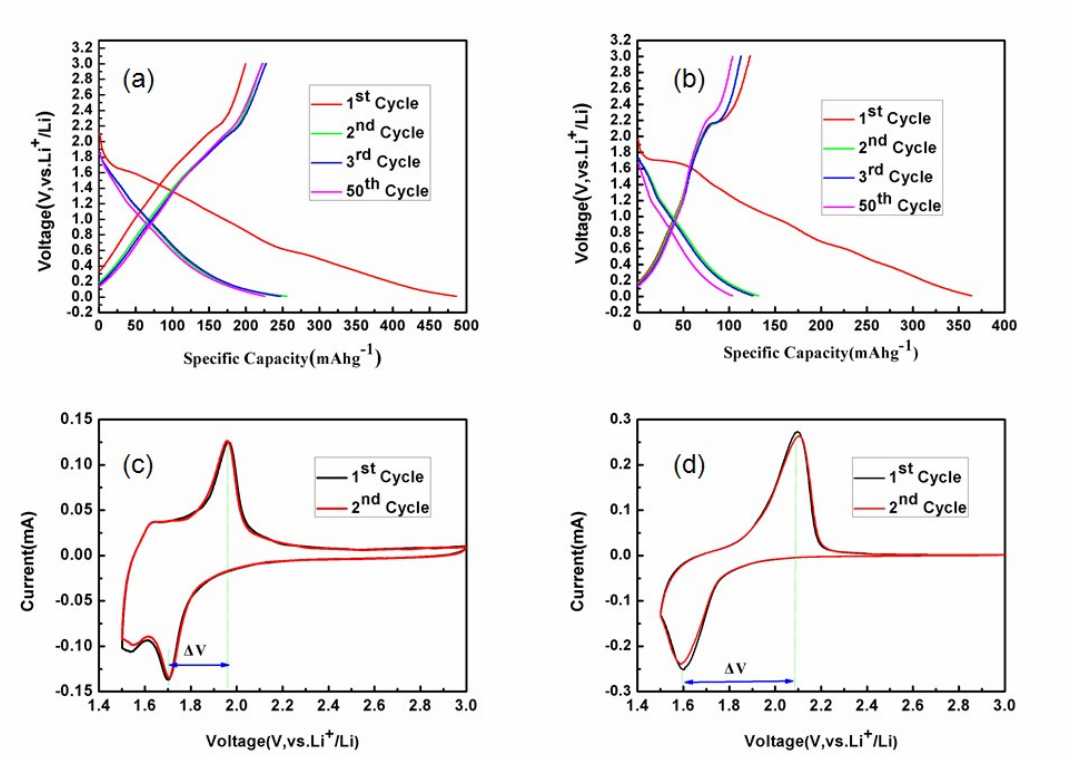

Fig 6. Discharge-charge voltage profiles of the FC-TiO_2 **(a)** and TiO_2 **(b)** electrodes for the 1st, 2 nd, 3rd and 50th cycles at a current rate of 3 C between 0.01 and 3.0 V. Cyclic voltammetries (CVs) of the FC-TiO_2 **(c)** and TiO_2 **(d)** electrodes at a scan rate of 0.02 mV s^{-1} for the first two scans.

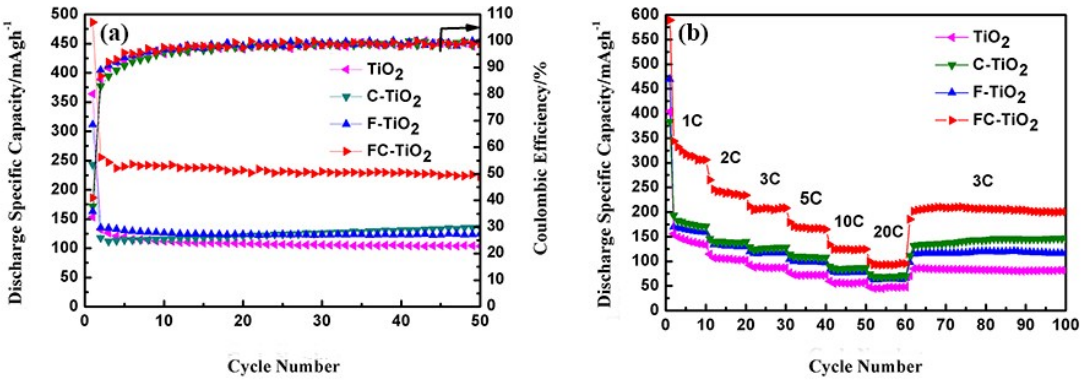

Fig 7. (a) Cycling performance (discharge capacities) at the current rate of 3 C between 0.01 and 3.0 V. **(b)** Cycling performance (discharge capacities) at various charge−discharge current rates of pure and modified TiO_2 between 0.01 and 3.0 V.

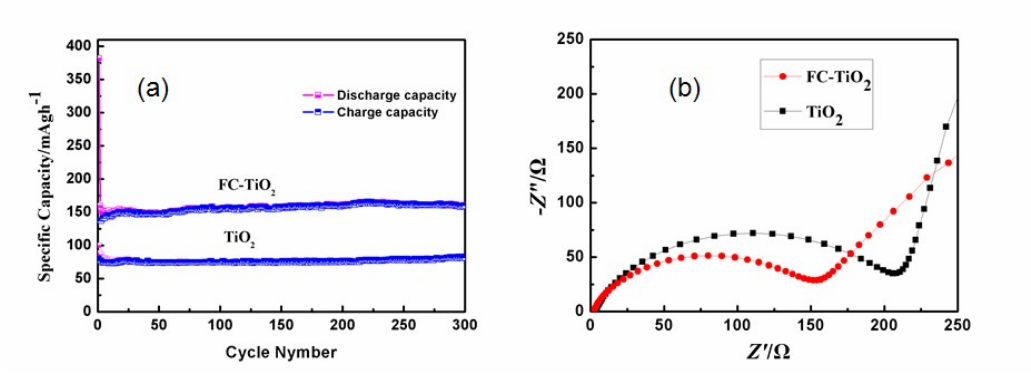

Fig 8. (a) Long-term cycling performance at the heavy current rate of 10 C between 0.01 and 3.0 V. **(b)** Electrochemical impendence spectra (EIS) of the FC-TiO_2 and TiO_2 electrodes.

533 **Table 1.** The comparison of different doped TiO_2 as anode for LIBs.

Anode	Current density (mA g^{-1})	Cycle Number	Capacity (mA h g^{-1})	Rfs（year）
N doped TiO_2	33.6	100	180.7	4 (2014)
Mesoporous TiO_2/Graphene/ Mesoporous TiO_2	20	100	237	16(2015)
graphene@mesoporous TiO_2 nanocrystals@carbon nanosheets	200	100	110	17(2015)
B doped TiO_2	1680	300	119.4	23 (2014)
C doped TiO_2	70	30	211	24 (2008)
Fe doped TiO_2	56	100	170	25 (2014)
F^- doped TiO_2	85	100	157	26 (2009)
F doped carbon coated mesoporous TiO_2	84	100	210	28(2015)
Carbon dots supported upon N doped TiO_2 nanorods	3350	1000	185	29 (2015)
Nb doped TiO_2	16.75	—	140	50 (2013)
Sn doped TiO_2	84	80	252.5	51 (2013)
Sn doped TiO_2	382	500	240	52 (2015)
Carbon/Fe doped anatase TiO_2 Composite	1700/510	300/50	158.6/222.4	In this article

534

535